Check for updates

Promotion of mixed protonic–electronic transport in La5.4WO11.1−δ membranes under H2S atmospheres†

S. Escolástico, [ID] *[ad] M. Balaguer,[a] C. Solís,[b] F. Toldra-Reig,[a] S. Somacescu,[c] U. Gerhards,[d] A. Aguadero,[e] K. Haas-Santo, [ID] [d] R. Dittmeyer [ID] [d] and J. M. Serra [ID] *[a]

Catalytic membrane reactors (CMR) based on H2-separation membranes can improve the performance of thermodynamically-limited reactions such as high-pressure steam methane reforming, ammonia cracking, non-oxidative aromatics production, and water gas shift reaction (WGS). In these industrial processes, the membrane surfaces are typically exposed to steam, CO_2, CO, H_2S, and hydrocarbons in combination with high temperatures. Therefore, the membrane materials require long-term thermo-chemical stability under the mentioned conditions. Stability in H_2S is of outstanding importance since its presence, even at ppm level, gives rise to substantial surface poisoning and decomposition of most materials. Here we characterize the influence of H_2S on the crystalline structure, lattice composition, and hydrogen-transport properties of La5.4WO11.1−δ, one of the reference protonic membrane materials. The incorporation of sulfide ions in the crystal lattice is ascertained from XRD, XPS, FESEM, WDS, EDS, and FIB-SIMS analyses. UV-vis spectroscopy and EIS measurements illustrate the effect of the incorporated sulfur in the transport properties, *i.e.*, vigorously promoting the electronic conductivity mediated by the concurrent partial reduction of tungsten cations (W^{6+}). The rise in electronic conductivity allowed an H_2 flux of 0.042 mL cm^{-2} min^{-1} to be reached at 700 °C for a ~700 μm-thick membrane, in contrast with negligible H_2 permeation in H_2S-free conditions.

Introduction

Catalytic membrane reactors (CMR) are becoming an exciting tool to improve the energy and carbon efficiency of different chemical processes and reduce operational and capital costs since they enable the combination of the reaction and separation in a single unit. CMR based on H2-separation membranes can be employed in several thermodynamically-limited reactions such as steam methane reforming, non-oxidative aromatics production, ammonia cracking, and water gas shift reaction (WGSR).[1] The H_2 separation increases the per-pass product yield of these reactions due to the equilibrium shift while a separate ultra-pure H_2 stream is produced.[2,3]

Protonic and mixed protonic–electronic conductors (MPEC) are promising materials applicable as H2-separation membranes in the abovementioned reactions due to their theoretical infinite H_2 selectivity and both thermo-chemical and mechanical stability under the required operation conditions.[4]

$BaCeO_3$, $BaZrO_3$, and their solid solutions are the most widely studied pure protonic conductors due to their high protonic conductivity. In this case, H_2 separation is driven by an applied voltage. By appropriately doping their structure with aliovalent cations or combining them with an electronic phase, important mixed protonic–electronic conductivity has been obtained with this kind of materials,[5–11] and this enables to utilize the differential pressure as the separation driving force instead of electric voltage. On the other hand, rare-earth tungsten oxides ($Ln_{6-x}WO_{12-y}$) have gained the researchers' attention due to their remarkable mixed conductivity and stability under harsh conditions.[12–16]

In the industrial process streams (CH_4, CO_2, NH_3) used in common catalytic reactions, different contaminants such as CO, amines, and H_2S can be found. Therefore, the long-term thermochemical stability under harsh conditions of the materials employed in the membranes can be challenging. The stability in H_2S requires special attention since its presence gives rise to substantial surface poisoning and decomposition of many materials.

aInstituto de Tecnología Química, Universitat Politècnica de València-Consejo Superior de Investigaciones Científicas, Avda. Los Naranjos, s/n, 46022, Valencia, Spain. E-mail: soesro@itq.upv.es; jmserra@itq.upv.es

bGerman Engineering Materials Science Centre (GEMS), Heinz Maier-Leibnitz Zentrum (MLZ), Helmholtz-Zentrum Hereon, 85748 Garching, Germany

c"Ilie Murgulescu" Institute of Physical Chemistry, Romanian Academy, Spl. Independentei 202, 060021 Bucharest, Romania

dIMVT, Karlsruhe Institute of Technology, 76344 Eggenstein-Leopoldshafen, Germany

eDepartment of Materials, Imperial College, London, SW7 2AZ, UK

† Electronic supplementary information (ESI) available. See DOI: https://doi.org/10.1039/d3ta01827j

17246 | *J. Mater. Chem. A*, 2023, 11, 17246–17256

This journal is © The Royal Society of Chemistry 2023

In recent years, promising protonic and MPEC materials have been tested under H_2S-bearing atmospheres. In general, $BaZrO_3$-based compounds present higher stability than $BaCeO_3$ (ref. 5 and 17) and, subsequently, incorporating Zr in $BaCeO_3$ improves the stability under H_2S-containing atmospheres.[18] $BaZr_{0.1}Ce_{0.7}Y_{0.2-x}Yb_xO_{3-\delta}$ was reported to be stable under an atmosphere composed of H_2 with 50 ppm of H_2S at 750 °C for 50 h.[19] $BaCe_{0.5}Zr_{0.4}Y_{0.1}O_{3-\delta}$ and $BaCe_{0.2}Zr_{0.7}Yb_{0.08}Ni_{0.02}O_{3-\delta}$ were exposed under an atmosphere containing 120 ppm of H_2S for 72 h, and no sulfide formation was observed.[20] Mortalò *et al.* studied the stability of the MPEC composite $BaCe_{0.65}Zr_{0.20}$-$Y_{0.15}O_{3-\delta}$–$Ce_{0.85}Gd_{0.15}O_{2-\delta}$.[21] $BaCe_{0.65}Zr_{0.20}Y_{0.15}O_{3-\delta}$ conductivity decreased under an H_2-rich stream comprising 2000 ppm of H_2S, although no structural changes were observed. Adding the $Ce_{0.85}Gd_{0.15}O_{2-\delta}$ phase improved the stability under H_2S atmospheres and the transport properties. The stability of $Ln_{6-x}WO_{12-y}$ (LWO) in H_2S has already been described.[13,14,22] A more exhaustive study reports the effect of the H_2S on the transport properties of the $Nd_{5.5}WO_{11.25-\delta}$ (NWO).[23] Total conductivity increases under H_2S atmospheres (2000 ppm) at temperatures above 600 °C, which was ascribed to the incorporation of S^{2-} ions in the oxide-ion sublattice, confirmed by SEM and WDS analysis. However, the specific effect of this incorporation, *i.e.*, the improvement of protonic or electronic conductivity, could not be ascertained.

On the other hand, LWO performance has been improved by partial substitution of the cation sites, reaching an important increase by partially doping the W position with Re and Mo.[14,24–27] In recent years, partial anion substitution appears to be another promising strategy. Improvement of transport properties and stability in LWO-based materials has also been reached by employing Cl and F.[28,29] In addition, S doping is extensively used in the so-called chalcogenides, which have attracted great interest due to their adjustable electronic structure, abundant active sites, low cost, environmental friendliness, and electrochemical performance.[30]

The present work aims to study the effect of H_2S-containing atmospheres on the transport properties of the protonic material $La_{5.4}WO_{11.1-\delta}$ (LWO). Crystal-structure changes of the compound and S^{2-} incorporation in the oxide lattice upon LWO exposure to H_2S are evaluated by X-ray diffraction, TEM, SEM, EDS, WDS, and XPS. In addition, the sulfur-atom profile along the material bulk is measured by FIB-SIMS. Transport properties of the material are measured by electrochemical impedance spectroscopy (EIS), whereas H_2 permeation is performed under both H_2S-free and containing atmospheres at 700 °C.

Experimental

$La_{5.4}WO_{11.1-\delta}$ powder was provided commercially by Cerpotech. Dense pellets (~98%) were achieved by uniaxial pressing at 100 MPa for 90 s and then sintered in air for 6 h at 1550 °C. The density of the various specimens was calculated by the Archimedes method by using a pycnometer and helium leakage test was used to confirm the gas tightness of the pellets. The powder for stability treatments was previously subjected to the same thermal cycle.

Structural and surface chemistry characterization

Initial and treated powders and pellets were characterized by X-ray diffraction. The measurements were carried out by a PANalytical Cubix fast diffractometer, using Cu K$\alpha_{1,2}$ radiation (λ_{α_1} = 1.5406 Å, λ_{α_2} = 1.5444 Å, I_2/I_1 = 0.5) and an X'Celerator detector in Bragg–Brentano geometry. The XRD patterns recorded from 2θ = 15° to 100° were analyzed using X'Pert HighScore Plus software. Crystalline phase(s) of the samples at room temperature were extracted from the patterns. Rietveld refinements of XRD patterns were performed using the FullProf software,[31] using a Si standard to measure the resolution file of the instrument. UV-vis spectra of the powders were recorded on a Varian 5000 UV-Vis-NIR spectrophotometer in the 200–800 nm range using $BaSO_4$ as a reference material and with a lamp change at 350 nm. Kubelka–Munk (K–M) theory was used to estimate the material's forbidden energy gap (E_g). This evaluation involves plotting the obtained ($h\nu F(RN)^{1/2}$) as a function of $h\nu$. The band gap, E_g, can be obtained by extrapolating a tangent line drawn in the point of inflection of the curve to zero, *i.e.*, the point of intersection with the $h\nu$ horizontal axis. Transmission electron microscope (TEM) investigation was carried out using a JEOL JEM-2100F (with an acceleration voltage of 200 kV) equipped with an EDX energy dispersive X-ray spectrometer. Surfaces and cross-fractures of the sintered pellets were analysed by a ZEISS Ultra-55 field-emission scanning electron microscope (FESEM), and a JEOL JXA-8530F microprobe, and elemental analysis was carried out with energy-dispersive X-ray spectroscopy (EDS) (INCA, Oxford) and Wavelength-dispersive X-ray spectroscopy (WDS), respectively. X-ray Photoelectron Spectroscopy (XPS) analysis was used to determine quantitatively the elements present on the outermost surface layer (<10 nm) and their chemical environment. XPS surface analysis was carried out on Quantera SXM equipment, with a base pressure in the analysis chamber of 10^{-9} torr. The X-ray source was Al Kα radiation (1486.6 eV, monochromatized), and the overall energy resolution was estimated at 0.65 eV by the full width at half maximum (FWHM) of the Au $4f_{7/2}$ line. In order to compensate for the unavoidable charging effect, the spectra were calibrated using the internal C 1s line (BE = 284.8 eV, C–C(CH)$_n$ bondings) of the adsorbed hydrocarbon on the sample surface. A dual beam (e^- and Ar^+ ion beams) was used to neutralize the charging effect in insulating samples. The errors in the quantitative analysis (relative concentrations) were estimated at ±5.0%, while the accuracy for Binding Energies (BEs) assignments was ±0.2 eV. The ISO-TC201 (SCA-Surface Chemical Analysis) committee recommendations[32] were followed by imposing constraints in the deconvolution process (the same procedure was followed for Shirley background, spin–orbit parameter, and the ratio of the intensities). In addition, a depth profile was performed utilizing FIB-SIMS (FIB200 SIMS Workstation, FEI, USA) to check the sulfur profiling along the bulk (1000 nm). The sample is bombarded by a focused gallium ions beam of 30 keV in an ultra-high vacuum chamber. The secondary ions produced by the beam are then analysed by a mass analyser (Hiden EQS 1000 detector). In this work, O^-, OH^-, S^-, and Pt^- negative ions were analyzed. For all the

This journal is © The Royal Society of Chemistry 2023

J. Mater. Chem. A, 2023, **11**, 17246–17256 | **17247**
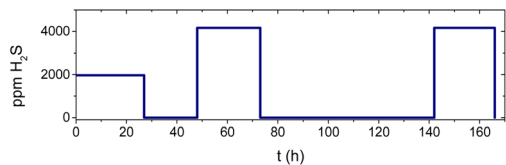
Fig. 1 H$_2$S concentration in the stream as a function of time at 700 °C.

measurements, a 10 × 10 μm square-shaped area was selected as the area of interest with a fixed current of 1070 pA. As sulfur secondary ion signal ($m/z = 32$) can be superimposed by $^{32}O^-$, a FIB-SIMS mass spectrum of the surface was carried out to exclude any $^{32}O^-$ contribution. Thus, a FIB-SIMS mass spectrum was performed for fresh and sulfur-exposed samples (LWO_I). Fig. S1† confirms that $^{32}S^-$ is the only secondary ion detected in the sample exposed to sulfur (LWO_I), as the fresh sample does not present any contribution due to $^{32}O^-$. Finally, the crater depth eroded by the primary beam is measured by a ZEISS Ultra-55 field-emission scanning electron microscope (FESEM).

EIS measurements under H$_2$S atmospheres

Electrochemical characterization of LWO under H$_2$S-containing atmospheres was performed by Electrochemical Impedance Spectroscopy (EIS) in a two-point four-wire configuration using Pt as electrodes (~20 μm) coated by screen printing. The input signal was 0 V DC–30 mV AC in the 1–5 × 10^5 Hz frequency range by using an EC-Lab SP-150 potentiostat equipped with a module for impedance analysis. First, under atmospheric pressure, EIS was measured under an atmosphere composed of humidified 10% H$_2$ in N$_2$ (2.5% H$_2$O) in the 700–400 °C range. Subsequently, an atmosphere comprising humidified 10% H$_2$ and ~2000 ppm (1973 ppm) H$_2$S in N$_2$ (2.5% H$_2$O) was fed into the reactor. Then, EIS measurements were performed from 400 to 700 °C, and the material remained for 24 h at each temperature under these harsh conditions. After 27 hours of feeding 2000 ppm H$_2$S at 700 °C, several cycles with (4000 ppm) and without H$_2$S were carried out (Fig. 1).

H$_2$ permeation measurements

LWO permeation measurements were performed on a double chamber quartz reactor sealed by a glass sealing tape K03 from Kerafol. The thickness of the LWO pellet used for these measurements was 770 μm. The temperature was maintained at 700 °C during all the experiment, and wet Ar was used as sweep gas (150 mL min^{-1}) on the permeation side.

First, H$_2$ permeation measurements were performed using a wet stream composed of 80 mL min^{-1} H$_2$ and 20 mL min^{-1} He free of H$_2$S as feed. Then, 40 mL min^{-1} of a mixture comprising 2500 ppm H$_2$S in H$_2$ and 10 mL min^{-1} He was employed as feed flow for 32 hours in order to incorporate sulfur in the sample. Subsequently, feed flow rates were increased to 80 mL min^{-1} of 2500 ppm H$_2$S in H$_2$, and 20 mL min^{-1} He, and H$_2$ permeation was measured. This stream was maintained for 24 hours, and then the H$_2$S feed was switched off for another 24 hours. These

two steps were repeated while H$_2$ permeation was constantly measured. The H$_2$ content in the sweep side was quantified using an online gas chromatograph (Agilent 7890B) equipped with five columns (2 MolSieve 13X, 2 Porapak Q and HP-Plot Q), and three detectors (2 TCD and FID). H$_2$ fluxes were corrected by subtracting the minor H$_2$ leak calculated by taking into account the He concentration detected in the sweep gas. This correction causes negligible J_{H_2} values at the beginning of the experiment, *i.e.*, a very low concentration of H$_2$ was detected in the permeate.

Before and after the H$_2$ permeation measurements, gas-tightness of the cells was also checked by SEM. Fig. S2† shows that samples are dense with some occluded porosity.

Results and discussion

Structural and surface chemistry characterization

Fig. 2 illustrates the XRD patterns of the as-prepared sample (LWO_AP) and the LWO powders treated 24 h with a humidified ($p_{H_2O} = 0.025$ atm) stream consisting of ~2000 ppm H$_2$S and 10% H$_2$ balanced N$_2$ at 500 °C (LWO_500) and 700 °C (LWO_700). The XRD pattern of the as-prepared LWO powder represents the features of a cubic fluorite (ICSD-189792).[33] With the H$_2$S treatment, the peaks become slightly wider and lower in intensity, and this effect is intensified as the treatment temperature increases, indicating loss of crystallinity. The LWO peaks shift to the left after the treatment at 500 °C, corresponding to an increase of the lattice parameter that could be ascribed to a substitution of the O by S or a change of the La/W ratio. The LWO peaks shift back to the right when treated at 700 °C, corresponding to a decrease in the lattice parameter, showing some extra peaks ascribed to La$_2$O$_2$S (ICSD-260145) and other non-identified phases. Table 1 summarizes the weight percentage of each phase found in the patterns, cell parameter, apparent size, strain, and density obtained by Rietveld refinement (see Fig. S3†). The obtained XRD data show that the cell parameter and grain size increase after the treatment at 500 °C. Both facts can be compatible with introducing S in the structure, substituting the O accompanied by a change in the La/W rate.[33] At 500 °C, no peaks from La$_2$O$_2$S could be detected by XRD analysis. However, the elemental analysis of the
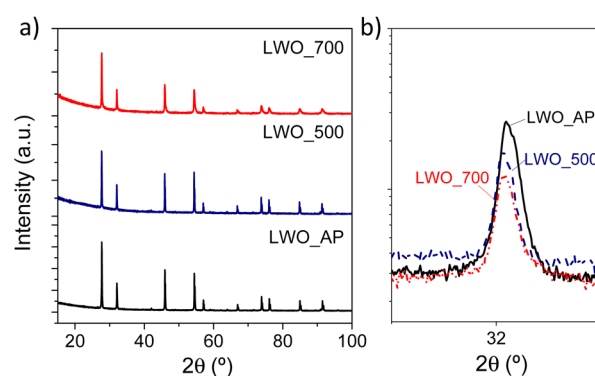

Fig. 2 Room temperature XRD patterns (a) and zoom in comparison of the (004) peak (b) of as prepared and LWO powders (LWO_AP) treated in wet H$_2$S at 500 °C (LWO_500) and 700 °C (LWO_700).

17248 | *J. Mater. Chem. A*, 2023, **11**, 17246–17256

This journal is © The Royal Society of Chemistry 2023

Table 1 Structural parameters and sulfur content of the LWO as prepared (LWO_AP) and treated at 500 (LWO_500) and 700 °C (LWO_700) 24 h with a stream consisting of ~2000 ppm H_2S and 10% H_2 saturated by water at room temperature (p_{H_2O} = 0.025 atm)

Sample	Composition	a/α (Å/°)	Size (Å)	Strain 10^{-4}%	Phase (wt%)	ρ (g cm^{-3})	S (E.A) (wt%)
LWO_AP	LWO	11.18809(15)	1806(2)		100	6.74	0
LWO_500	LWO	11.20157(24)	2733(3)		100	6.509	0.101
LWO_700	LWO	11.19608(48)	902	6.459	98(1)	6.46	0.666
	La$_2$O$_2$S	4.0481(43)			1.7(5)	5.77	

samples reveals the presence of sulfur (see Table 1), indicating that either the S is replacing the O in the LWO structure or the sulfur is present in the amorphous phase. When the sample is treated at 700 °C, more peaks are observed, some of which can be ascribed to the presence of around 2 wt% of La$_2$O$_2$S and the material presents a micro-strain that can be due to the effect of the S in the structure and the formation of the La$_2$O$_2$S.

Although previous studies report the formation of Ln$_2$O$_2$S only in samples with Ln$_2$O$_3$ impurities,[14,23] the formation of the oxysulfide from the reaction with the fluorite cannot be totally disregarded as no presence of La$_2$O$_3$ was detected at any stage. Besides, the LWO_700 cell parameter lies between the values of the LWO_AP and LWO_500, indicating a change in the La/W ratio of the LWO because of the formation of La$_2$O$_2$S. Furthermore, in this case, the size of the grains is much smaller, this points out that more than one process is taking place during the treatment, *i.e.* (1) the incorporation of the sulfur in the oxide lattice as concluded from the enlarged cell parameter; (2) the decrease of the crystalline size as corresponds to the broader peaks and (3) the formation of La$_2$O$_2$S on the surface favored by the high temperature.

To prove the incorporation of sulfur in the fluorite structure and the composition of the surface, a high-resolution XPS analysis was performed. Different LWO samples were analysed: as-sintered LWO pellets (LWO_AP) and LWO pellets treated for 24 hours under a humidified atmosphere (p_{H_2O} = 0.025 atm) composed of 10% H_2 and ~2000 ppm of H_2S balanced N$_2$ at 500 °C (LWO_500) and 700 °C (LWO_700) as aforementioned. The XPS analysis was performed in the 'as-received' state and after 0.5 min Ar$^+$ ion etching (subsurface region). The thickness removed from the material is estimated to be ~1 nm based on Baer's data on the sputter rates.[34] Under the mentioned Ar$^+$ ion etching, the surface contaminants (adsorbed hydrocarbons, weak OH groups, and oxidized sulfur group – SO$_x$) are removed mainly in the first two monolayers of atoms without significant alteration of the surface chemistry. Nevertheless, as even a gentle Ar$^+$ ion etching process can lead to a slight reduction of the cations, corrections were made by taking spectra on the as-sintered LWO (LWO_AP) sample as standard. This ensures that qualitative and quantitative assessments of the chemical species associated with La, W, and S are reliable.

The obtained spectra are displayed in Fig. 3 and 4, while the associated data are shown in Table 2 and Table 3. La 3d$_{5/2}$ photoelectron spectra show differences depending on the treatment temperature and in the as-received state and after Ar$^+$ ion etching (Fig. 3a and b, respectively). La cation is found in its

3+ oxidation state in all the samples as the corresponding binding energies (BEs) indicate, La 3d$_{5/2}$ ~834.0 ± 0.2 eV. Nevertheless, the spectra shape changes and shifts towards lower BEs with increasing treatment temperature. This effect is ascribed to the progressive building of bonding with sulfur related to its incorporation in the fluorite and also with the La$_2$O$_2$S formation and changes in the surface morphology.

The W electronic state exhibits significant modifications under the experimental conditions related to the presence of sulfur. Thus, in the as-received state, the W 4f$_{7/2}$ components, with BE ~35.3 eV (Fig. 3c), designate the fingerprint of the 6+ oxidation state characteristic of the lanthanum tungstate lattice. A close examination of the W 4f spectra after the Ar$^+$ ion etching (Fig. 3d) reveals an asymmetry on the lower BEs side, more pronounced at higher treatment temperature as a result of the reducing effect of H$_2$S exposure, and suggests the presence of 4+ oxidation state due to the interaction with sulfur.[35,36] Note that previous XPS studies made on Re and Mo doped Nd$_{5.5}$WO$_{11.25-\delta}$ showed that W cations do not suffer any reduction in 100% H$_2$ atmosphere at 900 °C.[14,37]

This effect was quantitatively assessed by spectral deconvolution. Fig. 4 shows the deconvolution for the different oxidation states of the W. The deconvolution of the W 4f spectrum for the LWO standard sample, after Ar$^+$ etching, highlights the presence of the induced W^{5+} (10.1%) and W^{4+} (2.9%) oxidation
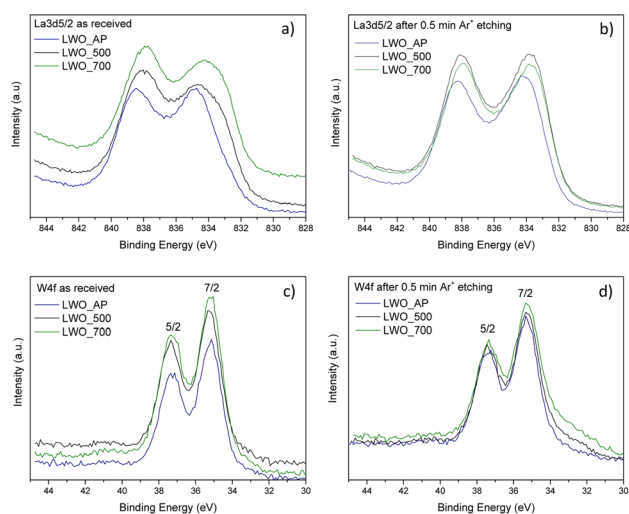

Fig. 3 Superimposed La 3d$_{5/2}$ (a and b) and W 4f (c and d) high-resolution XPS spectra in the as-received state and after 0.5 min Ar$^+$ ion etching for the samples LWO_AP, LWO_500, and LWO_700.
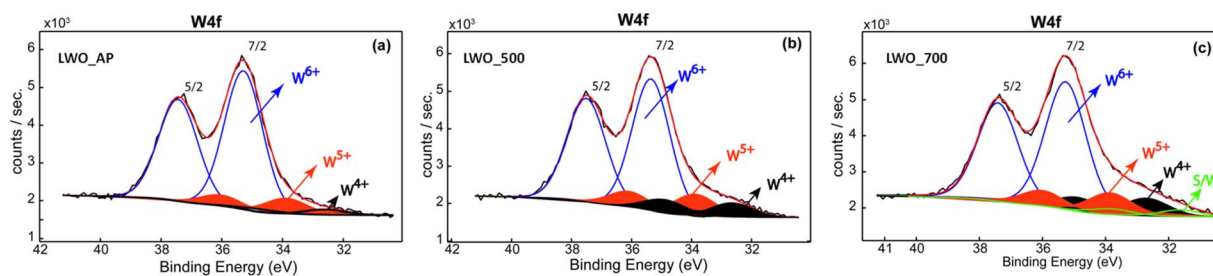
This journal is © The Royal Society of Chemistry 2023

J. Mater. Chem. A, 2023, **11**, 17246–17256 | **17249**

Fig. 4 Deconvolution of the W 4f high-resolution XPS spectra after 0.5 min Ar$^+$ ion etching for the samples LWO_AP (a), LWO_500 (b), LWO_700 (c).

Table 2 XPS data: the binding energies (eV) and the percentages of W chemical states (%) (after correction) in the as-received state and after 0.5 min Ar$^+$ ion etching (1 keV, (3 × 3) mm^2 rastered area)

Sample		Binding energy (eV)			Percentages of the W chemical states (%)			
		La 3d$_{5/2}$	W 4f$_{7/2}$	S 2p$_{3/2}$	W^{6+}	W^{5+}	W^{4+}	S/W^a
LWO	As received	834.9	35.2: W^{6+}	—	100	—	—	—
	After 0.5 min etching	834.3	35.2/33.9/32.6: W^{6+}/W^{5+}/W^{4+}		87.0	10.1	2.9	—
LWO_500	As received	834.7	35.2: W^{6+}	160.5: S–La/S–W ~168: S–O	100	—	—	—
	After 0.5 min etching	833.8	35.3/33.9/32.7: W^{6+}/W^{5+}/W^{4+}	160.5: S–La/S–W ~168: S–O	90.4	2.7	6.3	—
LWO_700	As received	834.4	35.3: W^{6+}	160.5: S–La/S–W	100	—	—	—
	After 0.5 min etching	833.7	35.2/33.9/32.7/31.6: W^{6+}/W^{5+}/W^{4+}/S/W	160.5: S–La/S–W	79.7	2.6	7.7	3.7

^{a} S/W (W 4f$_{7/2}$ = 31.5 eV) is ascribed to the surface W atoms attached to two sulfur atoms.

states on the surface. These lower oxidation states were created as a result of the Ar$^+$ ion sputtering even under mild experimental conditions. Therefore, the contributions of the 5+ and 4+ oxidation states corrected for the Ar$^+$ ion effect on the LWO_500, and LWO_700 samples were assessed.[38] Percentages of the chemical states for the W are shown in Table 2 (values shown for LWO_500 and LWO_700 correspond to the corrected values). The sample treated at 700 °C shows an extra peak at 31.6 eV (named S/W) that corresponds to W atoms attached to two sulfur atoms.[39,40]

The detection of sulfur on the sample surface as well as its chemistry on the outermost surface layer, is of particular interest. The S 2p photoelectron spectra for the samples in the as-received state (Fig. 5a and 11b) display two features: (a) the adsorbed oxidized sulfur group – SO$_x$ (S–O bond at BE ~168–169 eV), likely as SO$_4^{2-}$ ion, which is prominent for LWO_500; and (b) the bond S–La/S–W at BE ~160.4 eV that are dominant in the LWO_700 sample, assigned to the S^{2-} incorporation in the

fluorite and/or to the formation of the oxysulfide form (La$_2$O$_2$S). Ar$^+$ ion etching (1 keV, 3 × 3 mm^2 rastered area, 0.5 min sputter time) was also carried out to remove the contaminants in the first two monolayers without altering the surface chemistry (Fig. 5b and 11b). A sudden decrease in the surface's SO$_x$ percentage and an increase in the features associated with S–La/S–W bonds are observed. S–La/S–W bonds in LWO_500 increase from 57.0% to 85%, accompanied by the removal of the oxidized sulfur group from 43% to 15%, confined on the top of the surface. Note that no S 2p signal was detected for the LWO_AP sample.

Fig. 5c displays the superimposed high-resolution spectra recorded for the singlet O 1s. The spectra clearly show distinct shapes with prominent tails on the lower BEs side for the samples treated in the H$_2$S atmosphere. The component detected at BE ~529 eV is associated with the spectral fingerprint of the oxysulfide form, i.e., La$_2$O$_2$S.[41]

Table 3 summarizes the relative concentrations of elements in the samples after Ar$^+$ ion etching. Despite the formation of La$_2$O$_2$S, the data support the sulfur incorporation into the LWO lattice (an increase of the relative sulfur concentrations and detected S–La/S–W bonds) at 500 °C and 700 °C by substituting oxygen in the lattice. Furthermore, one can note a decreasing tendency of the oxygen relative concentrations (see Table 3) as S detected in the sample increases.

In summary, sulfur concentration increases with increasing treatment temperature and W reduction. These results agree with several studies where sulfidation of tungsten oxides was

Table 3 XPS data: relative element concentrations in the samples after 0.5 min Ar$^+$ ion etching (1 keV, 3 × 3 mm^2 scanned area)

Sample	Relative element concentrations (atom%)			
	O 1s	La 3d$_{5/2}$	W 4f	S 2p
LWO	73.9	22.0	4.1	—
LWO_500	68.0	25.0	4.5	2.5
LWO_700	65.6	25.3	4.8	4.3

17250 | J. Mater. Chem. A, 2023, **11**, 17246–17256

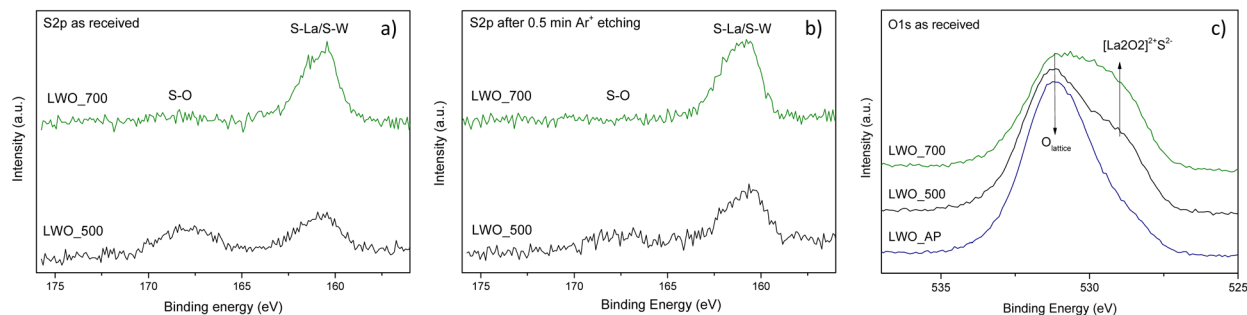This journal is © The Royal Society of Chemistry 2023

Fig. 5 The superimposed S 2p high-resolution XPS spectra in the as-received state (a) and after 0.5 min Ar⁺ ion etching (b) and the O 1s singlet in the as-received state (c) for the samples LWO_AP, LWO_500, and LWO_700.

carried out using an atmosphere of 10% H_2S in H_2.[42–44] The conclusions drawn in these studies are applicable here, explaining the W reduction and the partial sulfidation of LWO: (a) the reduction of W is exclusively attributed to the reaction with H_2S; (b) before oxygen–sulfur exchange can occur, a certain number of W atoms needs to be reduced; (c) once oxygen–sulfur exchange reactions occur, W is further reduced due to the W–S redox processes.

Transport properties of LWO under H_2S

The influence of H_2S on the transport properties of the LWO was studied by means of EIS measurements under H_2S-containing atmospheres. First, EIS measurements were performed under an atmosphere of wet 10% H_2 in N_2, from 700 °C to 400 °C with steps of 100 °C. Then, ~2000 ppm (1973 ppm) of H_2S were added to the gas stream, and EIS measurements were carried out 100 °C-stepwise from 400 to 700 °C, remaining 24 h at each temperature. The obtained impedance spectra are shown in Fig. S4.† Under an H_2S-free atmosphere, the spectra were fitted to the equivalent circuit (R1Q1)(R2Q2), assigned to the LWO bulk and the electrodes arc contributions, respectively. Under an H_2S-containing atmosphere, a third contribution appears, and the EIS spectra were fitted to the equivalent circuit (R1Q1)(R2Q2)(R3Q3) that corresponds to the bulk, grain boundary, and electrodes contribution as it was distinguished by their associated capacitances with values of 10^{-9}–10^{-8}, 10^{-8}–10^{-6} and 10^{-7}–10^{-6} F cm^{-2}, respectively. Moreover, at 700 °C, an additional real resistance appears at high frequencies and can be ascribed to the increase in the electronic contact resistance between Pt wires and electrodes due to the formation of PtS under the H_2S atmosphere as a result of the high temperature and long exposure time.[45] Then, at 700 °C, the equivalent circuit employed was R0(R1Q1)(R2Q2)(R3Q3) with associated capacitances of 10^{-8}–10^{-7}, 10^{-7}–10^{-6} and 10^{-4}–10^{-3} F cm^{-2}, respectively. EIS spectra with the corresponding contributions obtained from the fit can be seen in Fig. S5 and S6.† The total conductivities calculated from EIS fittings are depicted in Fig. 6a as a function of time on stream. At 400 and 500 °C, conductivity steeply decreases in the first hour of treatment and remains almost stable for at least 23 h. At 600 °C, conductivity also significantly decreases during the first hour, but then it increases with time and is not fully stabilized after 24 h. At 700 °

C, total conductivity increases with time from the beginning, and after 24 h, the material still does not reach the steady state. Fig. 6b compares the total conductivities after 24 h w/wo H_2S as a function of the reciprocal temperature. Below 700 °C, the total conductivity of LWO is lower under H_2S atmospheres. The apparent activation energy (EA) under H_2S-free conditions was 0.71 eV. Under the H_2S-containing atmosphere, two different slopes are observed, achieving an E_A value of 0.8 eV at low temperatures and 1.39 eV above 500 °C. However, it is worth recalling that conductivity was not stabilized after 24 h of H_2S exposure above 500 °C.

Fig. 6c plots the bulk and effective grain-boundary conductivities. Below 500 °C, the E_A value of the bulk conductivity (0.75 eV) in H_2S presence is similar to the corresponding value without H_2S, 0.62 eV. On the contrary, above 500 °C, apparent E_A for bulk conductivity increases to 2.04 under the H_2S-containing stream.

It has already been reported that lower La/W ratios give rise to higher electronic conductivities but lower total conductivities.[46] Then, the increase of the total conductivity is not related to the La/W ratio decrease because of the formation of La_2O_2S and can only be ascribed to the incorporation of S^{2-} in the crystal structure, as it is deduced from XRD and XPS results. The improvement of the total conductivity at high temperatures may be attributed to the transport of different species, i.e., (i) the transport of the S^{2-} ions through the structure; (ii) an increase of the proton and/or oxygen ion conductivity; and (iii) increase of the electronic conductivity.

Regarding the possibility of S^{2-} ions transport, the E_A value for S^{2-} transport is expected to be substantially higher than the corresponding value for O_2-hopping due to the larger size of the S^{2-} ion, i.e., 1.84 Å and 1.32 Å for S^{2-} and O^{2-}, respectively. Consequently, the transport of S^{2-} ion is expected to be slower, resulting in lower total conductivity. Improving the total conductivity observed at 700 °C under H_2S conditions enables us to rule out the role of S^{2-}-ion transport. On the other hand, the E_A value obtained above 500 °C in H_2S, 1.39 eV, is in the range of those obtained for NdWO-based materials at high temperatures where electronic and oxygen ion conductivities prevail.[13,14] This fact is confirmed by the reduction of the W cations (XPS measurements) that can boost electronic conductivity.
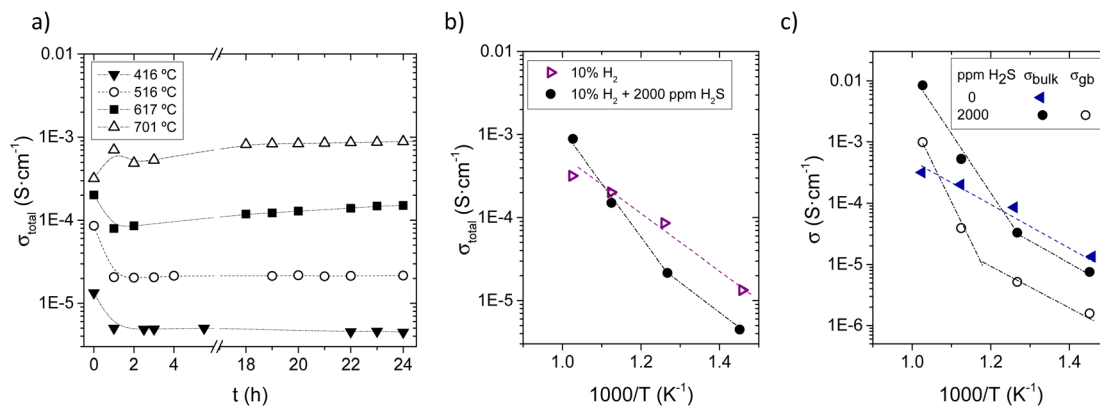
This journal is © The Royal Society of Chemistry 2023

J. Mater. Chem. A, 2023, **11**, 17246–17256 | **17251**

Fig. 6 Total conductivity of LWO sample under wet 10% H_2 and 2000 ppm H_2S balanced with N_2 atmosphere (a) as a function of time at different temperatures; comparison of the total conductivity (b); and bulk and grain boundary conductivities (c) as a function of the reciprocal temperature under wet 10% H_2 without and with 2000 ppm H_2S (after 24 hours).

UV-vis absorption experiments were performed to study the influence of the sulfur incorporation in the fluorite lattice in the band gap. The band gap reflects the energy difference between valence and conduction bands, being related to the extent of the electronic conductivity of the material. In fact, the optical band-gap energy is comparable to the thermal band gap associated with the formation of electron–hole pairs. Fig. 7 shows the room temperature UV-vis absorption spectra of the LWO. DFT calculations on doped fluorite-structured tungstates have determined it is an indirect bandgap.[47] A progressive addition of sulfur in the LWO induces a red shift of the absorption edge from 3.34 eV (LWO_AP) to 3.05 eV (LWO_700), indicating the promotion of the electronic transport through the oxide lattice.[48] The increase of the band-gap is not related to the La_2O_2S formation as its corresponding band-gap has been reported to be 4.9 eV.[49] Besides, this bandgap shift is consistent with previous studies where the bandgap of the $BaZrO_3$ was tuned, modifying the O/S ratio, going from 5 eV for $BaZrO_3$ to 1.7 eV for $BaZrS_3$.[30] These results validate the hypothesis of improved electronic conductivity by sulfidation of the LWO.

After 27 h at 700 °C under 2000 ppm H_2S (conductivity measurements shown in Fig. 6), the sample was exposed to
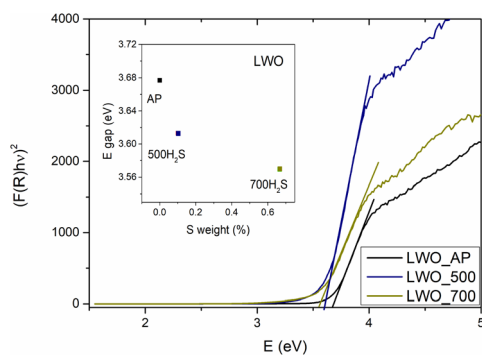
different atmospheres, as it is schematized in Fig. 1, while EIS measurements were continuously carried out. Fig. 8a plots the total conductivity (including the previous 27 h under 2000 ppm of H_2S), where solid data points at the end of each atmosphere correspond to the EIS spectra shown in Fig. 8b (Bode plot). The corresponding bulk and effective grain-boundary conductivities under these conditions are plotted in Fig. 9a, whereas Fig. 9b shows the polarization resistance of the electrodes. Total conductivity continuously increases regardless of the H_2S concentration. When H_2S is removed from the gas stream, the total conductivity does not decrease back to the initial value observed in wet H_2, but a change in the EIS spectra is observed. All the contributions (high, medium, and low resistances) decrease with time on the stream. Despite this gradual decrease in total resistance, it is observed that the relative contributions with and without H_2S differ. Bulk resistance contribution decreases when H_2S is fed, whereas grain boundary resistance increases, and the opposite behavior is observed for an H_2S-free atmosphere.

A closer look at the contributions to the total conductivity reveals that bulk conductivity steeply increases when H_2S is fed, then slightly decreases when H_2S is removed and increases again when 4000 ppm H_2S is fed in the stream. This behavior supports the observations of the narrower band gap and the W reduction, both contributing to electronic conductivity. On the
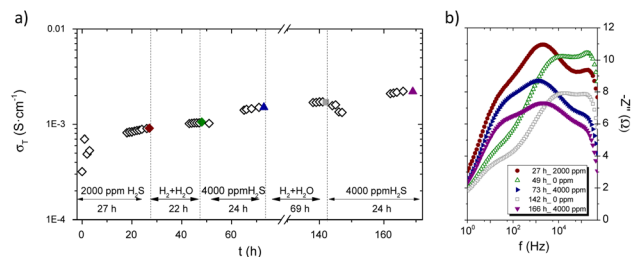

Fig. 7 Room temperature UV-vis absorption spectra: plot of $(F(R)h\nu)^2$ vs. photon energy of the LWO fresh (LWO_AP) and after the treatment at 500 (LWO_500) and 700 °C (LWO_700) under H_2S atmosphere. Inset: E_{gap} as a function of the % of sulfur detected in the sample.

Fig. 8 Total conductivity as a function of time for different H_2S concentrations (a) and Bode (b) plot for the conditions marked in (a) at 700 °C.

17252 | J. Mater. Chem. A, 2023, **11**, 17246–17256
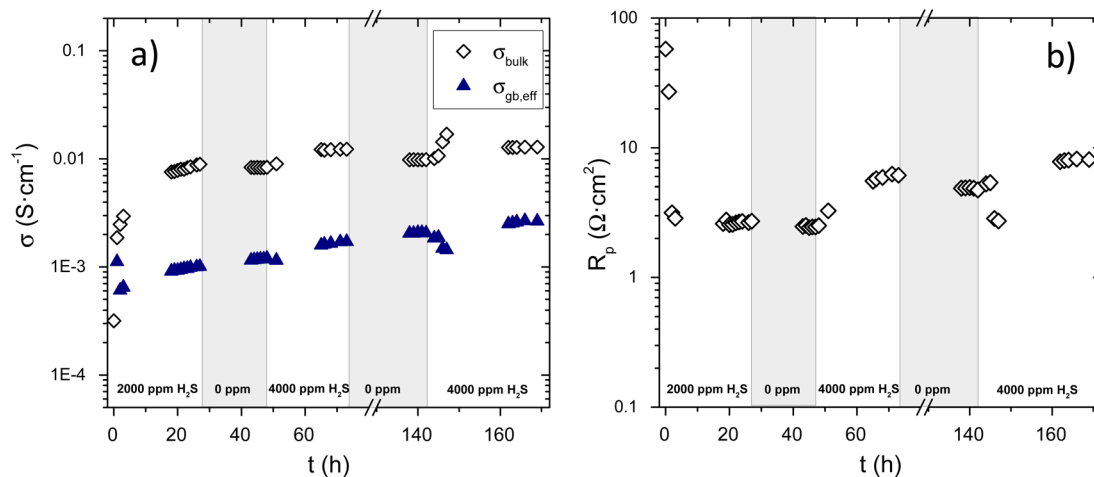
This journal is © The Royal Society of Chemistry 2023

Fig. 9 Bulk and grain boundary conductivities (a) and polarization resistance (b) at 700 °C as a function of time under different atmospheres: 2000 ppm (27 h), 0 ppm (22 h), 4000 ppm (24 h), 0 ppm (69 h) and 4000 ppm H_2S (24 h) in wet 10% H_2 balanced in N_2.

other hand, the effective grain-boundary conductivity slightly decreases for 2 h and continuously increases regardless of the H_2S concentration. In this case, this points out the sulfur enrichment of the grain boundaries. Regarding the electrodes, polarization resistance decreases at 700 °C and 2000 ppm H_2S, improving performance. This decrease is due to the so-called sulfur enhancement in fuel cells. This phenomenon causes the improvement of the fuel cells' performance due to the reduction of the interfacial resistance in the anodes at high temperatures and high concentrations of H_2S by forming a very thin layer of conductive sulfides on the oxide surface.[50] In contrast, an increase of the R_p is observed when 4000 ppm H_2S is fed, indicating the electrodes degradation at higher H_2S concentrations. The improved electrode performance under 2000 ppm H_2S contrasts with the real resistance ascribed to the electronic connection between Pt wires and electrodes. The employed Pt wires were previously exposed to H_2S atmospheres for several weeks giving rise to this degradation.

The structural and morphologic properties of the sample were characterized after EIS measurements. Fig. 10 shows the cross-section SEM image and the WDS maps for the main elements present in the sample. Sulfur was detected on the surface and homogeneously in the bulk of the LWO membrane; however, the concentration in the bulk was deficient to enable accurate quantitative analysis. High-sulfur concentration areas are mainly

located in the membrane surface and some occluded pores of the bulk, as previously observed for $Nd_{5.5}WO_{11.25-\delta}$ treated under similar conditions.[23] The surface-related areas with high-sulfur concentration exhibit low W concentrations, corresponding to the formation of La_2O_2S, as confirmed by the XRD analysis of the sample surface (Fig. S7†). On the other hand, the areas presenting the highest sulfur concentrations in the bulk do not match with low-W concentration areas. This further indicates the incorporation of the sulfide ion into the fluorite structure. Besides, a significant sulfur concentration is detected in the porous electrode's Pt grains, which is connected with a PtS layer formation.[45]

The combination of high-resolution XPS (Fig. 10b) and depth-profiling analysis (Fig. 11a) enables us to accurately quantify the sulfur distribution along the sample after electrochemical analysis. Fig. 10b shows the S 2p spectra for the sample after EIS measurements (LWO_I) in the as-received state and after Ar^+ ion etching. Similar to the sample treated at 700 °C (Fig. 5), S–La/W bonds (BE ~160.4 eV) increase from 30% to 87% (relative chemical concentrations) upon etching, whereas the percentage of S–O bond (BE ~168–169 eV) ascribed to SO_4^{2-} ion is reduced from 70% to 13%. The analysis of the W $4f_{7/2}$
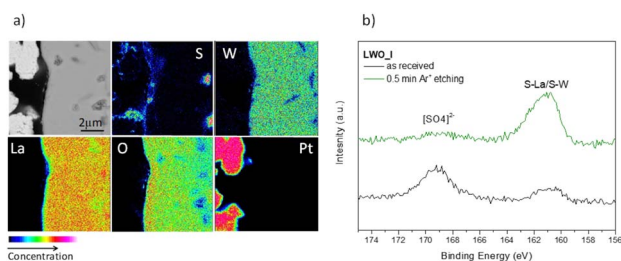

Fig. 10 BSE image and WDS map for S, W, La, O, and Pt (a) and S 2p XPS spectra after the EIS measurements (LWO_I) (b).
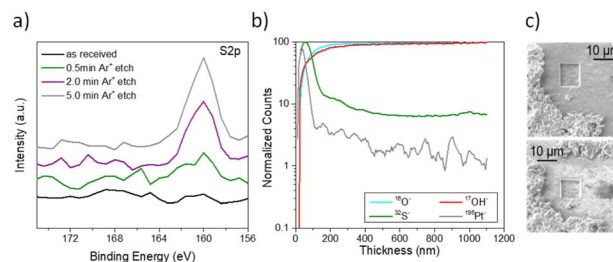

Fig. 11 S 2p XPS spectra for the LWO_I sample (note that 5 min sputter time (2 keV, (2 × 2) mm² rastered area) corresponds to about 30 nm sample depth) (a), FIB-SIMS depth profiling for the ions of interest: $^{16}O^-$, $^{17}OH^-$, $^{32}S^-$ and $^{195}Pt^-$ (b) and a micrograph of the 10 × 10 μm area analyzed with different tilt angles (c). Signals are collected with the Ga^+ sputter source at 30 keV and 1070 pA.

This journal is © The Royal Society of Chemistry 2023

J. Mater. Chem. A, 2023, **11**, 17246–17256 | **17253**

component after Ar$^+$ ion etching highlights the presence of the 7.7% W^{5+} and 13.9% W^{4+} oxidation states and a 3.8% corresponding to W atoms attached to two sulfur atoms (S/W).

In order to check the sulfur distribution on the surface of the LWO_I sample, a depth profiling experiment in four cycles was performed (Fig. 11a) under the following experimental conditions: 2 keV, (2 × 2) mm^2 rastered area, as received, 0.5 min, 2.0 min and 5.0 min sputter times. The superimposed survey S 2p XPS spectra outline the presence of sulfur in depth, associated with the complete removal of surface contaminants such as the adsorbed OH groups and hydrocarbons and carbon deposited during the manufacturing process. As a result, the sulfur peak increases in intensity through the surface, subsurface, and the bulk holding the characteristics of S–La/S–W chemical bonds, as shown in Fig. 11a.

LWO sample after the EIS measurements (LWO_I) was also analyzed by FIB-SIMS. Once confirmed that the ^{32}S$^-$ signal could be traced, a depth profiling study was conducted. Depth profiles of the secondary ion signals for ^{16}O$^-$, ^{17}OH$^-$, ^{32}S$^-$, and ^{195}Pt$^-$ are shown in Fig. 11b. Initially, the sulfur signal builds up to a peak, then decreases, reaching the steady state beyond the 400 nm depth. This sulfur signal remains constant through the bulk for a thickness of up to 1.2 μm. The sulfur presence along the bulk agrees with the depth profiling XPS experiment shown in Fig. 11a. As in the case of the sulfur, the Pt signal initially builds up to a peak before decreasing due to some mixing effect when the ion beam is applied and because Pt particles remain on the surface and the surroundings. Beyond 100 nm depth, the Pt signal is negligible.

Finally, H$_2$ permeation at 700 °C under H$_2$S-containing atmospheres was evaluated. First, H$_2$ permeation measurements were accomplished under H$_2$S-free conditions by feeding 80 mL min^{-1} H$_2$ and 20 mL min^{-1} He in the feed chamber. Permeation was negligible at this temperature due to the low electronic conductivity of the LWO in these conditions, as previously reported,[22] and only small quantities of He and H$_2$ were detected by GC, corresponding to a minor leak. Then, the 770 μm-thick membrane was treated with 40 mL min^{-1} of a mixture composed of 2500 ppm H$_2$S in H$_2$ and 10 mL min^{-1} of He for 32 h to incorporate sulfur in the membrane. After this treatment, H$_2$ permeation was measured by feeding 80 mL min^{-1} of the mixture H$_2$–H$_2$S and 20 mL min^{-1} of He. Fig. 12 depicts the H$_2$ permeation variation as a function of time on stream and the influence of the H$_2$S feeding. Red data points represent the negligible permeation before the H$_2$S. In contrast, an average value of 0.037 mL min^{-1} cm^{-2} was detected by feeding H$_2$S for 25 hours. By removing H$_2$S in the feed, H$_2$ flux decreases to 0.036 mL min^{-1} cm^{-2}. Then, H$_2$ flux increases once more when H$_2$S is added again, reaching a value of 0.042 mL min^{-1} cm^{-2}. In the last step, when H$_2$S is removed, H$_2$ flux (J_{H_2}) decreases, but a progressive increase is observed with time.

The permeation obtained under an H$_2$S atmosphere at 700 °C (around 0.04 mL min^{-1} cm^{-2}) is similar to that obtained for an S-free LWO membrane with a thickness of 900 μm at 850 °C. The increase of the H$_2$ flux at 700 °C under the H$_2$S atmosphere is associated with the increase in electronic conductivity achieved by incorporating sulfur in the fluorite structure. Sulfur
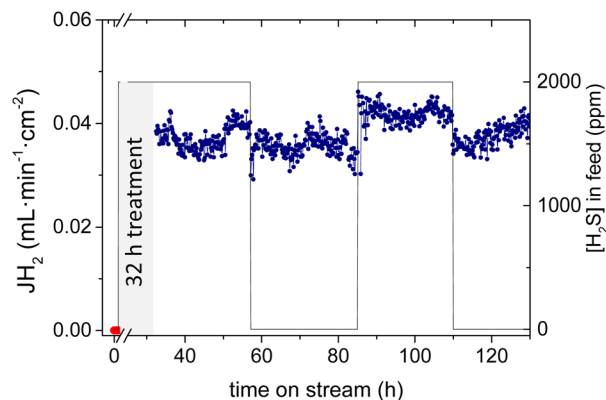

Fig. 12 H$_2$ permeation flux through 770 μm-thick LWO membrane as a function of time and H$_2$S concentration at 700 °C.

accommodation in the oxide lattice leads to the reduction of part of W^{6+} to W^{5+} and W^{4+}, which are not present under H$_2$S-free reducing conditions and, in turn, gives rise to the generation of additional oxygen vacancies. W reduction through reaction with H$_2$S enables to reach the level of electronic conductivity required for ambipolar H$_2$ permeation, as observed for Re and Mo-doped LWO with more reducible Re and Mo ions. In addition, incorporating sulfur in the oxygen sublattice causes a change in the electronic state that can give rise to an increase in the electronic conductivity of the material. In fact, assuming that H$_2$ transport occurs according to the ambipolar diffusion mechanism given by eqn (1) and assuming that the ionic conductivity ($\sigma_{H^+} + \sigma_{O^{2-}}$) corresponds to the first value obtained in Fig. 6 and that the increase in conductivity upon H$_2$S treatment is totally ascribed to the enhancement of the electronic conductivity of the material, the corresponding J_{H_2} at 700 °C is 0.037 mL min^{-1} cm^{-2} which is in full agreement with the J_{H_2} obtained in the permeation measurements.

$$J_{H_2} = \frac{RT}{4F^2L} \frac{(\sigma_{H^+} + \sigma_{O^{2-}})(\sigma_{e^-} + \sigma_h)}{\sigma_T} \ln \frac{p_{H_2}(\text{feed})}{p_{H_2}(\text{perm})} \quad (1)$$

On the other hand, when H$_2$S is removed from the feed, J_{H_2} values are nearly constant, and the slight decrease observed can be ascribed to minor changes in the feed flow rates. This behavior demonstrates that S^{2-} ions remain in the structure after 24 h under H$_2$S-free atmospheres, and W cations remain in a reduced state. The slight increase in J_{H_2} with time, in agreement with the EIS measurements shown in Fig. 8, may be related to incorporating more sulfur into the structure, i.e., reducing more W cations.

Conclusions

The evolution of the proton-conductor La$_{5.4}$WO$_{11.1-\delta}$ in the presence of H$_2$S at high temperatures was thoroughly studied. The incorporation of sulfur in the fluorite lattice is unambiguously demonstrated by XRD, FESEM, WDS and EDS, XPS, and FIB-SIMS analyses. The experimental results enabled quantitatively determining the distribution of the sulfur in the bulk and

17254 | J. Mater. Chem. A, 2023, 11, 17246–17256

This journal is © The Royal Society of Chemistry 2023

on the surface of the sintered LWO sample. The formation of La$_2$O$_2$S is detected after the treatment at 700 °C by XRD. However, the effects of the S incorporation in the material are already observable in the LWO cell after the treatment at 500 °C.

XPS analysis reveals the reduction of W^{6+} to W^{5+} and W^{4+} and the associated generation of oxygen vacancies, enhanced by temperature and uniquely promoted through the reaction with H$_2$S and the associated accommodation of S^{-2} in O^{-2} positions[42] since this reduction does not happen under H$_2$S-free reducing atmospheres. The incorporation of electrons in the conduction band of the crystal lattice was ascertained by detecting a decrease in the band gap and confirmed by continuous improvement of the conductivity at high temperatures. Both bulk and grain boundary resistivity decreases with time since the fraction of reduced W progressively increases in the grain interior and accumulates in the grain boundaries as the sulfur evolves. The extent of the sulfur incorporation was measured by FIB-SIMS, proving a sulfur-rich surface followed by a steady S concentration along the LWO grain interior.

The increase in electronic conductivity mediated by the coupled S incorporation and W reduction directly impact the H$_2$ permeation ability of the LWO membrane. Under 2000 ppm of H$_2$S, H$_2$ flux reaches a value of 0.042 mL min^{-1} cm^{-2} at 700 °C for a membrane thickness of 770 μm, in contrast with the negligible H$_2$ permeation under H$_2$S-free conditions at the same temperature. These results suggest that membranes composed of LWO could stand peaks of H$_2$S concentration at intermediate temperatures without losing their integrity while boosting their mixed-protonic–electronic conduction character. Further studies are needed to assess the effect of H$_2$S on the membrane surface and long-term stability, especially when using thin membranes with thicknesses of less than 100 μm. In addition, LWO membranes could be integrated into catalytic membrane reactors in different applications without the need to purify the feed stream. These findings show the excellent stability of LWO membranes under H$_2$S atmospheres and open the possibility of tuning the ambipolar conductivity by incorporating sulfide anions in the LWO oxygen sublattice.

Conflicts of interest

There are no conflicts to declare.

Acknowledgements

References

1 C. Duan, J. Huang, N. Sullivan and R. O'Hayre, Proton-conducting oxides for energy conversion and storage, *Appl. Phys. Rev.*, 2020, **7**, 011314.

2 H. Malerød-Fjeld, *et al.*, Thermo-electrochemical production of compressed hydrogen from methane with near-zero energy loss, *Nat. Energy*, 2017, **2**, 923–931.

3 S. H. Morejudo, *et al.*, Direct conversion of methane to aromatics in a catalytic co-ionic membrane reactor, *Science*, 2016, **353**, 563–566.

4 J. W. Phair and S. P. S. Badwal, Review of proton conductors for hydrogen separation, *Ionics*, 2006, **12**, 103–115.

5 S. Escolástico, *et al.*, Improvement of transport properties and hydrogen permeation of chemically-stable proton-conducting oxides based on the system BaZr1-x-yYxMyO3-δ, *RSC Adv.*, 2012, **2**, 4932–4943.

6 H. Matsumoto, *et al.*, Protonic-Electronic Mixed Conduction and Hydrogen Permeation in BaCe0.9−xY0.1RuxO3−α, *J. Electrochem. Soc.*, 2005, **152**, A488.

7 M. Cai, *et al.*, Preparation and hydrogen permeation of BaCe0.95Nd0.05O3−δ membranes, *J. Membr. Sci.*, 2009, **343**, 90–96.

8 X. Wei, J. Kniep and Y. S. Lin, Hydrogen permeation through terbium doped strontium cerate membranes enabled by presence of reducing gas in the downstream, *J. Membr. Sci.*, 2009, **345**, 201–206.

9 E. Rebollo, *et al.*, Exceptional hydrogen permeation of all-ceramic composite robust membranes based on BaCe0.65Zr0.20Y0.15O3-δ and Y- or Gd-doped ceria, *Energy Environ. Sci.*, 2015, **8**, 3675–3686.

10 E. Mercadelli, *et al.*, Chemical and mechanical stability of BCZY-GDC membranes for hydrogen separation, *Sep. Purif. Technol.*, 2022, **289**, 120795.

11 D. Montaleone, *et al.*, All-ceramic asymmetric membranes with superior hydrogen permeation, *J. Mater. Chem. A*, 2018, **6**, 15718–15727.

12 R. Haugsrud, Defects and transport properties in Ln6WO12 (Ln=La, Nd, Gd, Er), *Solid State Ionics*, 2007, **178**, 555–560.

13 S. Escolástico, M. Schroeder and J. M. Serra, Optimization of the mixed protonic-electronic conducting materials based on (Nd5/6Ln1/6)5.5WO11.25-δ, *J. Mater. Chem. A*, 2014, **2**, 6616–6630.

14 S. Escolástico, S. Somacescu and J. M. Serra, Tailoring mixed ionic-electronic conduction in H2 permeable membranes based on the system Nd5.5W1-xMoxO11.25-δ, *J. Mater. Chem. A*, 2015, **3**, 719–731.

15 A. López-Vergara, *et al.*, Effect of Preparation Conditions on the Polymorphism and Transport Properties of La6–xMoO12−δ (0 ≤ x ≤ 0.8), *Chem. Mater.*, 2017, **29**, 6966–6975.

16 S. Escolástico, *et al.*, Towards upscaling of La5.5 Wo11.25−δ manufacture for plasma spraying-thin film coated hydrogen permeable membranes, *Membranes*, 2020, **10**, 1–14.

17 J. Li, J.-L. Luo, K. T. Chuang and A. R. Sanger, Chemical stability of Y-doped Ba(Ce,Zr)O3 perovskites in H2S-containing H2, *Electrochim. Acta*, 2008, **53**, 3701–3707.

This journal is © The Royal Society of Chemistry 2023

J. Mater. Chem. A, 2023, **11**, 17246–17256 | **17255**

18 D. Medvedev, J. Lyagaeva, S. Plaksin, A. Demin and P. Tsiakaras, Sulfur and carbon tolerance of BaCeO3–BaZrO3 proton-conducting materials, *J. Power Sources*, 2015, **273**, 716–723.

19 L. Yang, *et al.*, Enhanced Sulfur and Coking Tolerance of a Mixed Ion Conductor for SOFCs: BaZr0.1Ce0.7Y0.2–xYbxO3–δ, *Science*, 2009, **326**, 126–129.

20 E. Forster, *et al.*, Stability of ceramic materials for H2 transport membranes in gasification environment under the influence of gas contaminants, *J. Eur. Ceram. Soc.*, 2016, **36**, 3457–3464.

21 C. Mortalò, *et al.*, Enhanced sulfur tolerance of BaCe0.65Zr0.20Y0.15O3-Δ-Ce0.85Gd0.15O2-Δ composite for hydrogen separation membranes, *J. Membr. Sci.*, 2018, **564**, 123–132.

22 S. Escolástico, C. Solís, T. Scherb, G. Schumacher and J. M. Serra, Hydrogen separation in La5.5WO11.25-δ membranes, *J. Membr. Sci.*, 2013, **444**, 276–284.

23 S. Escolástico, *et al.*, Chemical stability in H2S and creep characterization of the mixed protonic conductor Nd5.5WO11.25-Δ, *Int. J. Hydrogen Energy*, 2018, **43**, 8342–8354.

24 J. M. Porras-Vázquez, *et al.*, Effect of tri- and tetravalent metal doping on the electrochemical properties of lanthanum tungstate proton conductors, *Dalton Trans.*, 2016, **45**, 3130–3138.

25 E. Vøllestad, C. K. Vigen, A. Magrasó and R. Haugsrud, Hydrogen permeation characteristics of La27Mo1.5W3.5O55.5, *J. Membr. Sci.*, 2014, **461**, 81–88.

26 S. Escolastico, *et al.*, Enhanced H2 separation through mixed proton-electron conducting membranes based on La5.5W0.8M0.2O11.25-δ, *ChemSusChem*, 2013, **6**, 1523–1532.

27 S. Escolástico, C. Solís, R. Haugsrud, A. Magrasó and J. M. Serra, On the ionic character of H2 separation through mixed conducting Nd5.5W0.5Mo0.5O11.25−Δ membrane, *Int. J. Hydrogen Energy*, 2017, **42**(16), 11392–11399.

28 L. Chen, L. Liu, J. Xue, L. Zhuang and H. Wang, Tailoring hydrogen separation performance through the ceramic lanthanum tungstate membranes by chlorine doping, *J. Membr. Sci.*, 2019, **573**, 117–125.

29 L. Chen, L. Zhuang, J. Xue, Y. Wei and H. Wang, Tuning the separation performance of hydrogen permeable membranes using an anion doping strategy, *J. Mater. Chem. A*, 2017, **5**, 20482–20490.

30 S. Perera, *et al.*, Chalcogenide perovskites – an emerging class of ionic semiconductors, *Nano Energy*, 2016, **22**, 129–135.

31 J. Rodríguez-Carvajal, Recent advances in magnetic structure determination by neutron powder diffraction, *Phys. B*, 1993, **192**, 55–69.

32 C. J. Powell, Summary of ISO/TC 201 Standard: XXIX. ISO 20903: 2006—Surface chemical analysis—Auger electron spectroscopy and X-ray photoelectron spectroscopy—methods used to determine peak intensities and information required when reporting results, *Surf. Interface Anal.*, 2007, **39**, 464–466.

33 T. Scherb, *et al.*, Nanoscale order in the frustrated mixed conductor La5.6WO12-δ, *J. Appl. Crystallogr.*, 2016, **49**, 997–1008.

34 D. R. Baer, *et al.*, Comparison of the sputter rates of oxide films relative to the sputter rate of SiO2, *J. Vac. Sci. Technol., A*, 2010, **28**, 1060–1072.

35 B. Deepthi, *et al.*, Structure, morphology and chemical composition of sputter deposited nanostructured Cr–WS2 solid lubricant coatings, *Surf. Coat. Technol.*, 2010, **205**, 565–574.

36 Y. Koçak, Y. Akaltun and E. Gür, Magnetron sputtered WS2; optical and structural analysis, *J. Phys.: Conf. Ser.*, 2016, **707**, 12028.

37 S. Escolástico, S. Somacescu and J. M. Serra, Solid state transport and hydrogen permeation in the system Nd5.5W1-xRexO11.25-δ, *Chem. Mater.*, 2014, **26**, 982–992.

38 E. Paparazzo, XPS analysis of iron aluminum oxide systems, *Appl. Surf. Sci.*, 1986, **25**, 1–12.

39 D. R. Mullins and P. F. Lyman, Sulfur-induced changes in the W(001) surface core level shift, *Surf. Sci.*, 1993, **285**, L473–L478.

40 A. V. Naumkin, A. Kraut-Vass, S. W. Gaarenstroom and C. J. Powell, NIST X-ray Photoelectron Spectroscopy Database, *NIST Stand. Ref. Database 20, Version 4.1*, 2012, DOI: **10.18434/T4T88K**.

41 N. T. Lau, M. Fang and C. K. Chan, The role of SO2 in the reduction of NO by CO on La2O2S, *J. Catal.*, 2007, **245**, 301–307.

42 A. J. van der Vlies, G. Kishan, J. W. Niemantsverdriet, R. Prins and T. Weber, Basic Reaction Steps in the Sulfidation of Crystalline Tungsten Oxides, *J. Phys. Chem. B*, 2002, **106**, 3449–3457.

43 A. J. van der Vlies, R. Prins and T. Weber, Chemical principles of the sulfidation of Tungsten oxides, *J. Phys. Chem. B*, 2002, **106**, 9277–9285.

44 B. Frühberger, M. Grunze and D. J. Dwyer, Surface chemistry of H2S-sensitive tungsten oxide films, *Sens. Actuators, B*, 1996, **31**, 167–174.

45 M. Liu, P. He, J. L. Luo, A. R. Sanger and K. T. Chuang, Performance of a solid oxide fuel cell utilizing hydrogen sulfide as fuel, *J. Power Sources*, 2001, **94**, 20–25.

46 A. Magrasó and R. Haugsrud, Effects of the La/W ratio and doping on the structure, defect structure, stability and functional properties of proton-conducting lanthanum tungstate La28−xW4+xO54+δ. A review, *J. Mater. Chem. A*, 2014, **2**, 12630–12641.

47 H. Li, *et al.*, Crystal structure, electronic structure, and optical and photoluminescence properties of Eu(III) ion-doped Lu6Mo(W)O12, *Inorg. Chem.*, 2011, **50**, 12522–12530.

48 F. Cheviré, *et al.*, Tunability of the optical properties in the Y6(W,Mo)(O,N)12 system, *Solid State Sci.*, 2009, **11**, 533–536.

49 R. Vali, Electronic, dynamical, and dielectric properties of lanthanum oxysulfide, *Comput. Mater. Sci.*, 2006, **37**, 300–305.

50 Z. Cheng, *et al.*, From Ni-YSZ to sulfur-tolerant anode materials for SOFCs: electrochemical behavior, in situ characterization, modeling, and future perspectives, *Energy Environ. Sci.*, 2011, **4**, 4380–4409.

17256 | *J. Mater. Chem. A*, 2023, **11**, 17246–17256

This journal is © The Royal Society of Chemistry 2023